The effect of 10 at.% Al addition on the hydrogen storage properties of the Ti0.33V0.33Nb0.33 multi-principal element alloy

Nayely Pineda-Romero, Matthew Witman, Vitalie Stavila, Claudia Zlotea

The effect of 10 at.% Al addition on the hydrogen storage properties of the $Ti_{0.33}V_{0.33}Nb_{0.33}$ multi-principal element alloy

Nayely Pineda-Romero[1], Matthew Witman[2], Vitalie Stavila[2] and Claudia Zlotea[1]*

[1]*Univ Paris Est Créteil, CNRS, ICMPE, UMR 7182, 2 rue Henri Dunant, 94320 Thiais, France*

[2] *Sandia National Laboratories, Livermore, California 94551, United States*

* Corresponding author email: claudia.zlotea@cnrs.fr

ABSTRACT

We report here a thorough study on the effect of 10 at.% Al addition into the ternary equimolar $Ti_{0.33}V_{0.33}Nb_{0.33}$ alloy on the hydrogen storage properties. Despite a decrease of the storage capacity by 20 %, several other properties are enhanced by the presence of Al. The hydride formation is destabilized in the quaternary alloy as compared to the pristine ternary composition, as also confirmed by machine learning approach. The hydrogen desorption occurs at lower temperature in the Al-containing alloy relative to the initial material. Moreover, the Al presence improves the stability during hydrogen absorption/desorption cycling without significant loss of the capacity and phase segregation. This study proves that Al addition into multi-principal element alloys is a promising strategy for the design of novel materials for hydrogen storage.

KEY WORDS:

Multi-principal element alloys, metal hydrides, neutron diffraction, thermodynamic properties, machine learning

INTRODUCTION

Hydrogen has a strong ability to be a replacement for fossil fuels, but an important research effort is still needed to find efficient storage materials for practical devices [1]. H_2 can be stored in solid-state form as metal hydrides which have the advantages of being safer as compared to gas storage, and achieve higher volumetric capacities that exceed those of liquid H_2 [2]. Metal hydrides are a well-known class of materials for solid-state H_2 storage, but they have not yet fulfilled all the needs for profitable and efficient storage devices.

Recently, a new class of materials known as multi-principal element alloys (MPEA) or high-entropy alloys (HEA), have captured significant attention because of their interesting hydrogen storage properties [3]. The MPEA are substitutional solid solutions with simple crystalline structures (*bcc, fcc, hcp*) and show large lattice distortion (δ) due to the variation in the atomic radii of its component atoms. This latter parameter is interesting for hydrogen storage since large lattice distortion might open large interstitial sites to accommodate hydrogen at high hydrogen to metal (H/M) ratios, as demonstrated by the TiVZrNbHf composition [4].

Several studies on the hydrogen storage properties of MPEAs/HEAs containing refractory elements (such as Ti, V, Nb, Zr, Hf, Ta) have been reported, showing a single phase *bcc* solid solution with a hydrogen uptake around 2.0 H/M and 2-3.2 wt.% [2,3,5–8]. In order to increase the gravimetric capacity of hydrogen storage, the use of lightweight elements, such as Mg and Al, has been proposed in past studies [3,5]. One promising lightweight metal is Mg, which reaches a hydrogen uptake of 7.7 wt.% in the hydride MgH_2 [9]. Mg-containing HEAs have been studied but their capacities are typically low *i.e.*, 0.3 wt.%-1.6 wt.% [10–12]. In a recent study, however, Montero *et. al*. have been reported the novel composition $Mg_{0.10}Ti_{0.30}V_{0.25}Zr_{0.10}Nb_{0.25}$, which forms a single-phase *bcc* and absorbs hydrogen very quickly at 25°C forming a *fcc* hydride with a hydrogen uptake of 1.7 H/M (2.7 wt.%). The H_2

absorption/desorption process is fully reversible with a stable capacity of 2.4 wt.% during cycling without any phase segregation [5].

Another interesting lightweight metal is Al, which has a gravimetric hydrogen storage capacity of 10 wt.% as hydride (AlH_3) and a volumetric density of around 148 g H_2/L at 25°C, being twice higher than that of liquid H_2. It also displays a low enthalpy of reaction, around 7 kJ/mol H_2, and rapid hydrogen desorption kinetics below 100°C. However, it has drawbacks: impossible regeneration of Al in a cost-effective way, direct formation from metallic Al and H_2 gas requires high pressures (above $2.5x10^4$ bar) and the stable oxidation layer formation at Al surface [13]. Due to its potential to decrease the density of alloys, Al has been used in the design of lightweight HEAs. Stepanov *et al*. reported the composition $Al_{0.266}Ti_{0.251}V_{0.245}Nb_{0.238}$, which crystalizes in a single-phase *bcc* solid solution and possesses a density of 5.59 g cm^{-3}[14]. Furthermore, several reports have attributed the Al addition in HEAs as a stabilizer of the *bcc* crystal structure [15,16]. Recently, Montero *et al*. reported the effect on the hydrogen storage properties of 10 at. % Al addition in the refractory MPEA $Ti_{0.325}V_{0.275}Zr_{0.125}Nb_{0.275}$[17]. The new $Al_{0.10}Ti_{0.30}V_{0.25}Zr_{0.10}Nb_{0.25}$ alloy adopts an initial *bcc* structure which transforms into a *bct* after the hydride formation with a maximum hydrogen uptake of 1.6 H/M (2.6 wt. %). Additionally, hydrogen desorption temperature was decreased by 110 °C and the cycling stability improves as compared to the Al-free alloy. Therefore, Al addition in refractory alloys seems to be a promising method for improving the hydrogen storage properties of refractory MPEAs/HEAs.

Moreover, to rationalize the design of novel and high-performing materials in the vast compositional space of MPEAs, new approaches are currently being developed, such as data-driven predictions facilitated by machine/statistical learning (ML) [18,19]. This new approach stands as an alternative to traditional computational methods and aims rapidly down select promising compositions from the practically infinite composition space of MPEAs. To complete the research loop, these predicted properties, such as capacity and reaction thermodynamics, need laboratory verification. Nonetheless, if strategies for hydride destabilization *i.e.,* via Al addition, can be quantitatively assessed

a priori, the scope of necessarily time-consuming experiments can be quickly narrowed to maximize successful realization of hydrides with desired properties.

In this work, we report on the synthesis, the physicochemical properties, and the hydrogen storage performances of a novel MPEA containing Al and refractory elements, $Al_{0.10}Ti_{0.30}V_{0.30}Nb_{0.30}$. Our goal is to highlight the effect of Al addition in the ternary composition $Ti_{0.33}V_{0.33}Nb_{0.33}$ when synthesized by the same method. Thus, we have carried out a systematic comparative study among the pristine $Ti_{0.33}V_{0.33}Nb_{0.33}$ alloy and the Al-containing counterpart, $Al_{0.10}Ti_{0.30}V_{0.30}Nb_{0.30}$. This includes the use of well-known laboratory techniques as well as large-scale experiments, such as *in-situ* neutron diffraction. A previously developed ML model is applied for the prediction of the thermodynamic parameters and their dependence on Al addition.

MATERIALS AND METHODS

The $Al_{0.10}Ti_{0.30}V_{0.30}Nb_{0.30}$ and $Ti_{0.33}V_{0.33}Nb_{0.33}$ alloys were synthetized by the electric arc melting method from bulk pieces of Ti (99.99% pure, Alfa Aesar), V (99.9% pure, NEYCO Vacuum&Materials), Nb (99.95% pure, Alfa Aesar) and Al (99% pure, STREM Chem). Ti, V and Nb metals were pre-alloyed in an arc furnace under Ar atmosphere (around 300 mbar) and recast 16 times, flipping the ingot in between each melting to achieve good homogeneity. Because Al has a low melting point and to avoid loss of material, it was added after the TiVNb pre-alloy and melted under the same conditions mentioned before and recast 8 times by turning over the ingot between each melting step.

The hydrogenation process was carried out using the Sievert's method consisting of a manual homemade manometric device with thermostatically calibrated volumes. The stainless-steel sample holder was filled with around 400-500 mg of sample cut in small pieces, using metal gaskets to prevent gas leaking, and then sealed and connected to the Sievert's apparatus. Prior to starting the hydrogenation process, an activation procedure was carried out by exposing the sample at 400°C under

dynamic vacuum (~3x10^{-5} mbar) overnight. For the absorption kinetics the sample holder is placed in a water bath at isothermal conditions (25°C) and the sample is exposed to 60 bar of H_2. For the acquisition of Pressure-compositions isotherms (PCI's) at high temperatures we have used a resistive furnace. The mass of the samples is measured carefully before hydrogenation to calculate the storage capacity using the real gas state equation for H_2 (GASPAK Version 3.32, Horizon Technologies). For absorption/desorption cycling experiments, the absorption was performed at 25 °C under 60 bar H_2, whereas the desorption is performed at 400°C under secondary vacuum (~3x10^{-5} mbar) for 12 hours.

The crystalline structure of the samples was studied by laboratory powder X-ray diffraction (XRD) using a D8 Advance Bruker diffractometer (Cu Kα radiation λ=1.5406Å, Bragg-Brentano Geometry).

The hydrogen desorption was analysed by thermal desorption spectroscopy (TDS) using a homemade instrument with a quadrupole mass spectrometer QMS, as described previously [20]. The procedure consists of loading about 10 mg of the hydride sample into the sample holder and then connecting to the quadrupole mass spectrometer working under secondary vacuum (~1x10^{-6}mbar). The desorption profile was recorded by heating the sample at a constant rate of 5°C/min.

In-situ powder neutron diffraction (nD) experiments were performed at the D1B beamline (λ=1.28 Å) of the Institute Laue-Langevin, Grenoble, France. The fully deuterated sample was placed inside a silica tube connected to a vacuum equipment (base pressure ~ 10^{-5} mbar). A constant heating rate of 1°C/min was applied from around 42 - 46 °C to 400 °C under dynamic vacuum. The 2θ domain ranges from 10 to 100 °C and the pressure of the desorbed gas was recorded during deuterium desorption with the help of a vacuum gauge. Additionally, *ex-situ* nD experiments were carried out on the initial deuterated materials using a vanadium sample holder at room temperature.

The lattice parameters of different phases were determined from XRD and *ex-situ* nD patterns using the Rietveld refinement method implemented in the Fullprof software (Thompson-Cox-Hastings

pseudo-Voigt function for the peak shape) or the CELREF unit cell refinement of powder diffraction data software (http://ccp14.cryst.bbk.ac.uk/solution/unitcellrefine/index.html).

The microstructure was analysed by scanning electron microscope (SEM) using a Zeiss Merlin instrument equipped with an EDX (Energy-Dispersive X-ray Spectroscopy) detector from Oxford Instruments. The samples were embedded in an epoxy resin, then finely polished and finally coated with 1.5-2.5 nm Pd layer. For elemental analysis an accelerated electron voltage of 10 keV was used and the element quantification was performed using Al(K), Ti(K), V(K) and Nb(L) signals. The experiments were carried out for the as-cast, after first hydrogenation and after cycling samples.

RESULTS AND DISCUSSIONS

The $Ti_{0.33}V_{0.33}Nb_{0.33}$ and $Al_{0.10}Ti_{0.30}V_{0.30}Nb_{0.30}$ alloys synthesized by the arc-melting method adopt a single-phase *bcc* lattice (*Im-3m*), as confirmed by XRD (Figure 1a and 1b). The lattice parameters are a_{bcc} = 3.211(1) Å and a_{bcc} = 3.195(1) Å for the ternary and quaternary alloy, respectively (Table 1). The lattice parameter of the ternary alloy is in good agreement with earlier reported value for the same composition [21]. The addition of Al into the equimolar ternary alloy reduces the lattice parameter that can be understood by the decrease of the Ti content, which has the largest atomic size among all containing elements: 1.46 Å, 1.43 Å, 1.43 Å and 1.39 Å for Ti, Nb, Al and V, respectively [22]. This behaviour has been also reported in our previous study reporting the effect of 10 at.% Al addition in Ti-V-Zr-Nb [17]. Moreover, the lattice distortion is reduced from 4.42% to 4.2% with the addition of Al because its atomic radius (1.43 Å [22]) is close to that of Ti and Nb (1.46 Å, 1.43 Å, respectively [22]), leading to the decrease of atom size disparity in the quaternary alloy. Another parameter that is reduced with the Al addition is the valence electron concentration (VEC) from 4.67 to 4.5. The values of lattice distortion and VEC from both samples are in the range (δ < 6.6%, VEC < 6.87) where single-phased *bcc* solid solutions are reported [23,24] .

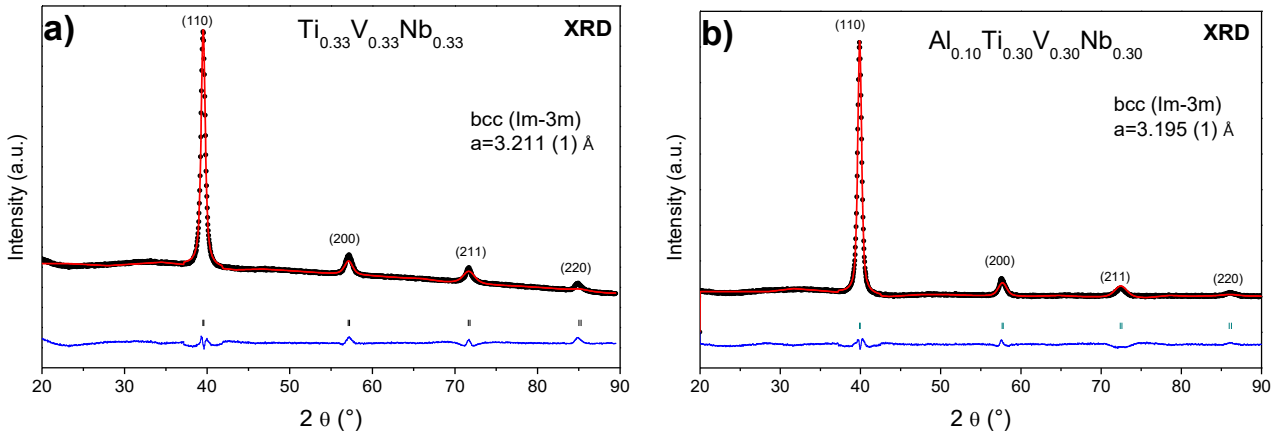

Figure 1. *Rietveld refinement analysis of the X-Ray diffraction (XRD) patterns (λ = 1.5406Å) for the (a) as-cast $Ti_{0.33}V_{0.33}Nb_{0.33}$ and (b) as-cast $Al_{0.10}Ti_{0.30}V_{0.30}Nb_{0.30}$ alloys.*

Furthermore, the density of the alloy decreases by Al addition from 6.42 to 6.03 g/cm^3 from ternary to quaternary composition, respectively. This finding agrees with the already well documented strategy to reduce the density of HEAs by Al addition. Senkov *et al.* reported a density decrease of around 10% in $CrMo_{0.5}NbTa_{0.5}TiZr$ by complete Cr substitution with Al and in HfNbTaTiZr by partial Hf substitution with Al [16]. Also, Stepanov *et al*. reported a density of 5.59 g/cm^3 in the lightweight AlNbTiV alloy [14].

Composition	Form	Phase structure	Space group	Lattice Parameter (Å)	Analyzed by
$Ti_{0.33}V_{0.33}Nb_{0.33}$	As-cast	*bcc*	Im-3m	3.211(1)	XRD
$Ti_{0.33}V_{0.33}Nb_{0.33}H_{2.0}$	Hydride	*fcc*	Fm-3m	4.443(1)	XRD
$Ti_{0.33}V_{0.33}Nb_{0.33}D_{2.0}$	Deuteride	*fcc*	Fm-3m	4.432(1)	nD
$Ti_{0.33}V_{0.33}Nb_{0.33}$	Desorbed	*bcc*	Im-3m	3.207(5)	XRD
$Ti_{0.33}V_{0.33}Nb_{0.33}H_{1.8}$	Hydride after 11th cycle	*fcc*	Fm-3m	4.450(2)	XRD
$Al_{0.10}Ti_{0.30}V_{0.30}Nb_{0.30}$	As-cast	*bcc*	Im-3m	3.195 (1)	XRD
$Al_{0.10}Ti_{0.30}V_{0.30}Nb_{0.30}H_{1.59}$	Hydride	*fcc*	Fm-3m	4.375(5)	XRD
$Al_{0.10}Ti_{0.30}V_{0.30}Nb_{0.30}D_{1.6}$	Deuteride	*fcc*	Fm-3m	4.358(1)	nD
$Al_{0.10}Ti_{0.30}V_{0.30}Nb_{0.30}$	Desorbed	*bcc*	Im-3m	3.197(5)	XRD
$Al_{0.10}Ti_{0.30}V_{0.30}Nb_{0.30}H_{1.5}$	Hydride after 10th cycle	*fcc*	Fm-3m	4.348(9)	XRD

Table 1. *Lattice parameters of the $Ti_{0.33}V_{0.33}Nb_{0.33}$ and $Al_{0.10}Ti_{0.30}V_{0.30}Nb_{0.30}$ compositions: as-cast, hydride, deuteride, desorbed and hydride after 10-11th absorption/desorption cycle.*

The hydrogen absorption PCI measurements reveal the existence of two plateaus for $Ti_{0.33}V_{0.33}Nb_{0.33}$ (Figure 2a) and $Al_{0.10}Ti_{0.30}V_{0.30}Nb_{0.30}$ (Figure 2b). The first plateau ends at around 0.8 - 0.9 H/M with very low equilibrium pressure, below the detection limits of the pressure transducer (10^{-2} bar), whereas the second plateau at higher pressure reaches a maximum capacity of 2.0 H/M (3.2 wt.%) and 1.59 H/M (2.6 wt.%) for $Ti_{0.33}V_{0.33}Nb_{0.33}$ and $Al_{0.10}Ti_{0.30}V_{0.30}Nb_{0.30}$, respectively.

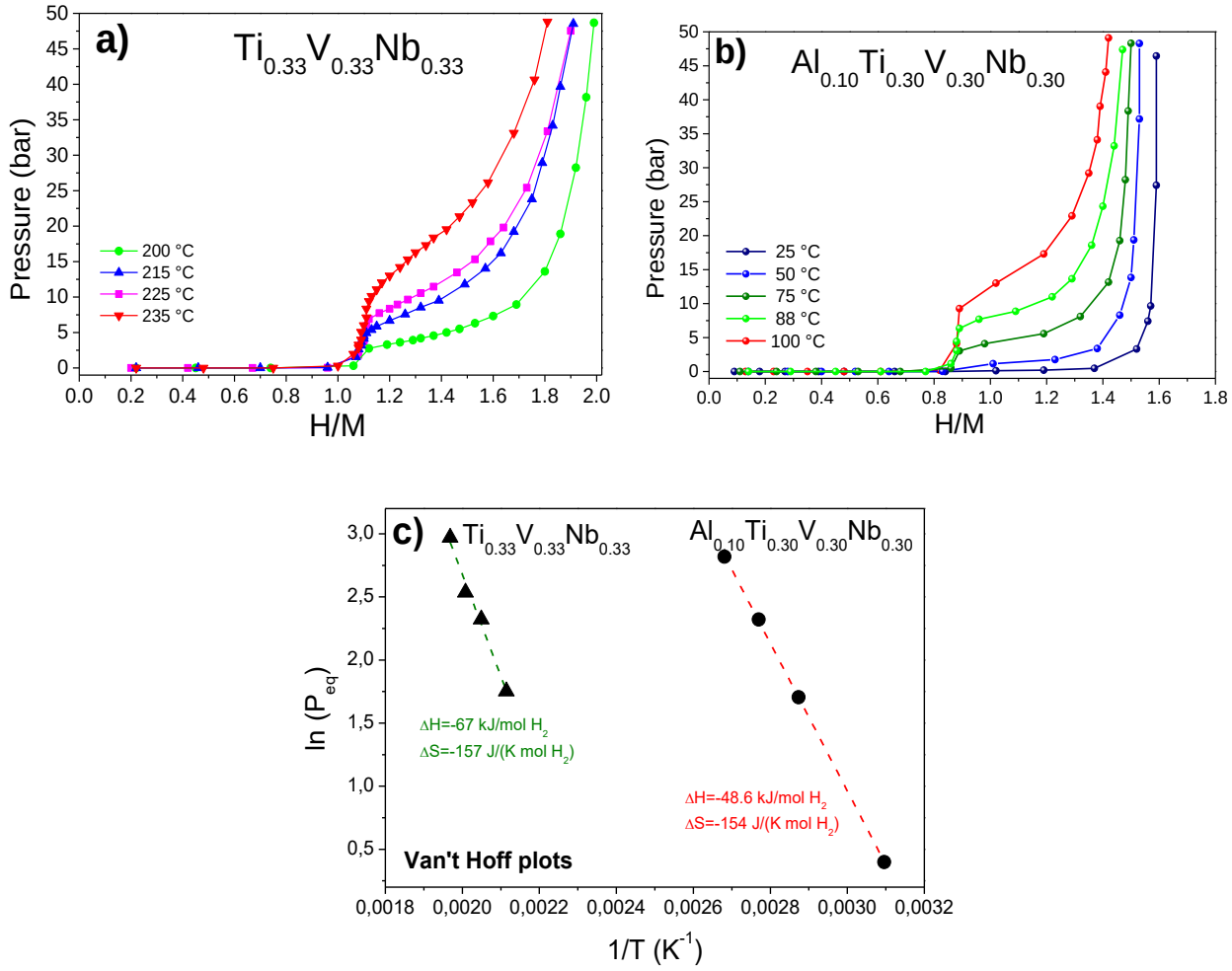

Figure 2. *Pressure-composition isotherms of (a) $Ti_{0.33}V_{0.33}Nb_{0.33}$ and (b) $Al_{0.10}Ti_{0.30}V_{0.30}Nb_{0.30}$. (c) Van't Hoff plots for both compositions.*

The addition of 10 at. % Al in the $Ti_{0.33}V_{0.33}Nb_{0.33}$ alloy decreases the hydrogen storage capacity by 20 % from 2.0 to 1.59 H/M, comparably with the previously reported tendency for $Ti_{0.325}V_{0.275}Zr_{0.125}Nb_{0.275}$ [17] (the capacity reduces from 1.75 to 1.6 H/M by the addition of 10 at. % Al).

The maximum capacity of 2.0 H/M for the ternary alloy agrees well with the already reported value for the equimolar TiVNb [21]. Despite the capacity decrease, the presence of Al flattens the plateaus in the PCI curves, which is a desirable attribute for practical storage applications.

The thermodynamic properties of the dihydride formation for both compositions have been determined from the variation of the equilibrium pressure of the second plateau with temperature *i.e.*, by using the van't Hoff approach (Figure 2c). The experimental change in the enthalpy and entropy values for the absorption reaction are listed in Table 2 together with those from close compositions reported previously for the formation of the *fcc* dihydride [25,26]. The predicted values from the ML approach are also given. The addition of 10 at. % Al in the ternary composition leads to a thermodynamic destabilisation since the ΔH of dihydride formation decreases from around -67 to approximately -49 kJ/mol H_2 for $Ti_{0.33}V_{0.33}Nb_{0.33}$ and $Al_{0.10}Ti_{0.30}V_{0.30}Nb_{0.30}$, respectively.

Composition	ΔH_{abs} (kJ/mol H_2)	ΔS_{abs} (J/K·mol H_2)	References
$Ti_{0.33}V_{0.33}Nb_{0.33}$	-67 (5) (exp.) -58 (ML)	-157 (11)	This work
$Al_{0.10}Ti_{0.30}V_{0.30}Nb_{0.30}$	-48.6 (1.0) (exp.) -51 (ML)	-154 (2)	This work
$Ti_{0.283}V_{0.283}Nb_{0.283}Cr_{0.15}$	-67	-172	[25]
$Ti_{0.25}V_{0.25}Nb_{0.25}Cr_{0.25}$	-51.6	-129.3	[27]
$Ti_{0.3206}V_{0.3206}Nb_{0.3206}Ni_{0.038}$	-64	-164	[25]
$Ti_{0.3176}V_{0.3176}Nb_{0.3176}Co_{0.047}$	-67	-174	[25]
$Ti_{0.25}V_{0.25}Nb_{0.25}Zr_{0.25}$	-67.6	-90.3	[26]

Table 2. *Thermodynamic properties for hydrogen absorption reaction of the $Ti_{0.33}V_{0.33}Nb_{0.33}$ and $Al_{0.10}Ti_{0.30}V_{0.30}Nb_{0.30}$ alloys together with results for close compositions reported earlier. The present experimental values are determined from van't Hoff equation and the predicted ones from ML model proposed earlier.*

Despite the rather large differences between the experimental ΔH and the predicted value by ML for the ternary alloy, the results for the quaternary composition are in very good agreement. Moreover, the measured hydride destabilization trend by Al addition is well predicted by the ML model : ΔH is calculated -58 and -51 kJ/mol H_2 for the ternary and the quaternary alloys, respectively, confirming the

robustness of the earlier proposed ML approach for metal hydrides [18,19]. Figure SI3 also shows the ML predicted trend in ΔH and maximum H/M capacity as a function of Al content, validating this approach for assessing new MPEA hydrides. Interestingly, hydrides broadly exhibit a strong positive correlation of ΔH on $\bar{v}_{pa}$ (a composition-derived, volume-related descriptor identified as the most important feature in the ML model, see [18,19] for details). Yet the ML model correctly predicts the opposite trend in this system (i.e., ΔH is negatively correlated with $\bar{v}_{pa}$ in Figure SI3), indicating the model is successfully utilizing non-trivial secondary design rules for thermodynamic property prediction [18,19]. The measured values of the ΔS are close to the expected value for the entropy of H_2 free gas *i.e.*, -130 J/K·mol H_2. The large error bar in the experimental thermodynamic values of the ternary alloy which is mainly due to the sloped plateaus which is not the case for the quaternary one.

It is interesting to compare the present results to previously reported values of MPEAs with close compositions [25–27]. Most of the alloys in Table 2 show similar thermodynamic properties indicating very stable hydrides. The values of $Ti_{0.3206}V_{0.3206}Nb_{0.3206}Ni_{0.038}$ and $Ti_{0.3176}V_{0.3176}Nb_{0.3176}Co_{0.047}$ agree well with our results for the ternary composition, as expected since these MPEAs contain only small amount of Ni and Co. As for the effect of the addition of other elements in the ternary TiVNb, it seem that the presence of 25 at.% Cr in the equimolar $Ti_{0.25}V_{0.25}Nb_{0.25}Cr_{0.25}$ leads to a destabilisation of the hydride [27], as also demonstrated in our case. However, the effect of Cr addition into TiVNb is less clear since quite different thermodynamic properties have been reported for the 15 at.% Cr in $Ti_{0.283}V_{0.283}Nb_{0.283}Cr_{0.15}$ [25].

It is obvious from PCI curves that both alloys show the formation of an intermediate monohydride (with capacity around 0.8-0.9 H/M), as also encountered for other multiprincipal-element-alloys such as, TiZrNbHfTa [8] and Ti-V-Nb-*X* (*X* = Cr, Ni, Co) [25]. To investigate the hydrogen absorption induced phase transformation, the hydrogenation process was stopped at several points on the PCI curve at room temperature: in the middle of the first plateau (0.4-0.5 H/M), at the end of the

first plateau (0.8-0.9 H/M), in the middle of the second plateau (1.2-1.3 H/M) and at the end of the second plateau (1.6-2.0 H/M). The crystalline structures during these hydrogenation steps were determined by XRD (Figure 3). Both compositions show the presence of two distinct *bcc* phases with slightly different lattice parameters in the middle of the first plateau (at around 0.4-0.5 H/M). One phase is a *bcc* solid solution with hydrogen whereas, the other phase is the *bcc* intermediate monohydride. At the end of the first plateau (0.8-0.9 H/M) the alloys have been completely transformed into intermediate *bcc* monohydrides. For higher hydrogen content both materials start forming a dihydride, as proven by the presence of the *bcc* monohydride coexisting with the *fcc* dihydride phase in the middle of the second plateau (1.2-1.3 H/M). Finally, the materials are fully converted to dihydride at the end of the second plateau with maximum capacity (1.6-2.0 H/M). The Rietveld refinements of the *fcc* dihydrides for both compositions are shown in Figure SI4 and their corresponding lattice parameters are listed in Table 1. Therefore, both alloys react similarly with hydrogen following the sequence of phase transformation: *bcc* solid solution → *bcc* monohydride → *fcc* dihydride.

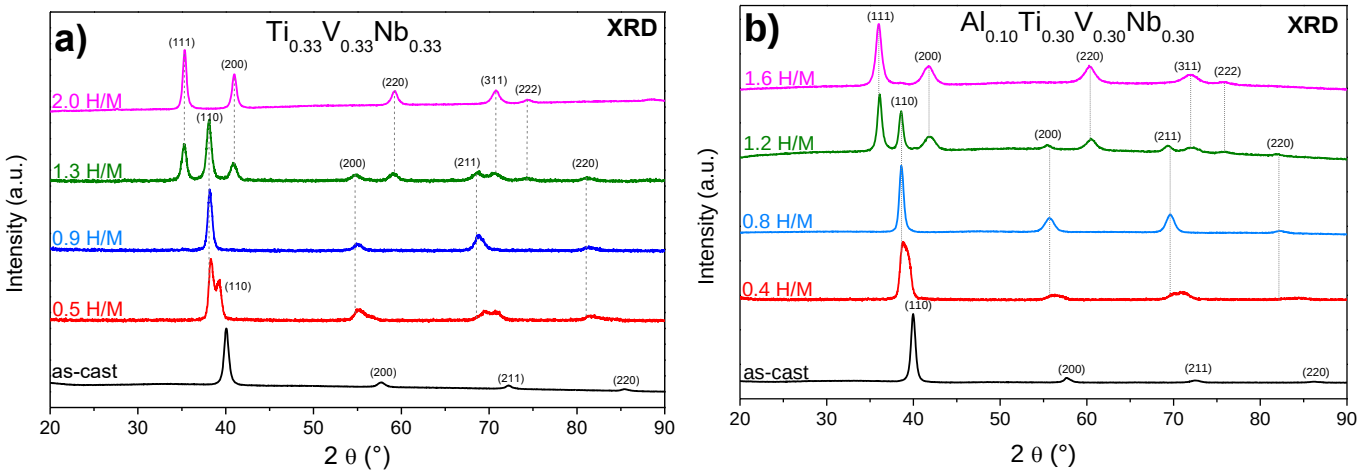

Figure 3. *XRD patterns (λ = 1.5406 Å) at several stages of the hydrogenation process for a) $Ti_{0.33}V_{0.33}Nb_{0.33}$ and b) $Al_{0.10}Ti_{0.30}V_{0.30}Nb_{0.30}$.*

The EDX-SEM chemical mapping analysis of the $Ti_{0.33}V_{0.33}Nb_{0.33}H_{2.0}$ and $Al_{0.10}Ti_{0.30}V_{0.30}Nb_{0.30}H_{\sim 1.6}$ hydrides are shown in Figure 4. Generally, a homogeneous distribution of the elements throughout the alloys is observed and the overall chemical compositions of the $Ti_{0.33}V_{0.33}Nb_{0.33}H_{2.0}$ (Table 3) and $Al_{0.10}Ti_{0.30}V_{0.30}Nb_{0.30}H_{\sim 1.6}$ (Table 4) are in good agreement with the nominal ones. Both alloys show

dendritic microstructures with slightly different chemical compositions between the dendritic and the interdendritic zones. The Ti and V distributions seem homogenous in the ternary alloy whereas the dendrites are slightly enriched in Nb, though the deviation from the average composition is minor (1-2 at.%). Similar results have been reported earlier for the equimolar TiVNb composition [21]. In the quaternary alloy, the Ti, V and Al distributions are homogenous but the interdendritic regions are slightly enriched in Al/Ti/V, though the deviation from average composition is very small (1-2%). These small chemical modulations in the atomic concentration are assumed to be due to the solidification process, as reported in other refractory HEAs [17].

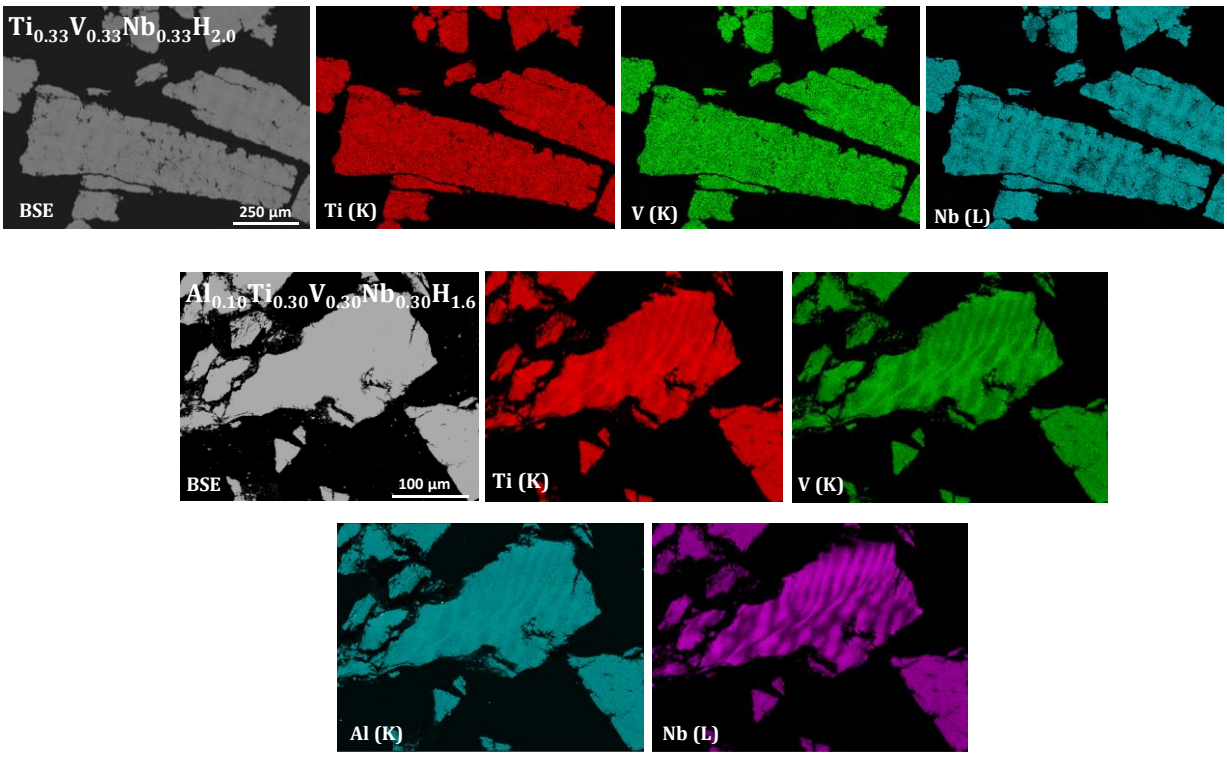

Figure 4. *EDX-SEM chemical mapping analysis of the hydrides* $Ti_{0.33}V_{0.33}Nb_{0.33}H_{2.0}$ *and* $Al_{0.10}Ti_{0.30}V_{0.30}Nb_{0.30}H_{1.6}$.

Element	Nominal (at. %)	Cycles	Overall average (at. %)	Nb rich region (at. %)	Nb poor region (at. %)
Ti (K)	33	1	32.8 (0.6)	32.5 (0.4)	33.5 (0.6)
		11	32.5 (1.2)	32 (0.9)	33.8 (0.8)
V (K)	33	1	32.8 (0.6)	32.5 (0.4)	33.6 (0.5)
		11	32.5 (1.5)	31.9 (1.3)	34.1 (0.8)
Nb (L)	33	1	34.4 (1.1)	35 (0.4)	32.9 (1.1)
		11	35.1 (2.6)	36.1 (2.1)	32.1 (1.5)

Table 3. *Atomic percentage concentrations of the $Ti_{0.33}V_{0.33}Nb_{0.33}H_{2.0}$ hydride after 1st and 11th cycles.*

Element	Nominal (at. %)	Cycles	Overall average (at. %)	Nb rich region (at. %)	Nb poor region (at. %)
Al (K)	10	1	9.7 (0.3)	9.6 (0.2)	10.3 (0.4)
		10	9.7 (0.3)	9.6 (0.3)	10.1 (0.2)
Ti (K)	30	1	29.6 (1.0)	29.3 (0.5)	31.5 (0.3)
		10	29.5 (0.7)	29.3 (0.6)	30.6 (0.5)
V (K)	30	1	29.5 (1.1)	29.2 (0.7)	31.1 (1.2)
		10	29.5 (0.9)	29.2 (0.7)	30.8 (0.3)
Nb (L)	30	1	31.2 (2.3)	32 (1.4)	27 (1.8)
		10	31.3 (1.8)	31.9 (1.4)	28.6 (1.0)

Table 4. *Atomic percentage concentrations of the $Al_{0.10}Ti_{0.30}V_{0.30}Nb_{0.30}H_{1.6}$ hydride after 1st and 10th cycles.*

The structural properties of the dihydride phases of both compositions were characterized by *ex-situ* neutron diffraction (nD) using deuterium instead of hydrogen. The nD patterns of $Ti_{0.33}V_{0.33}Nb_{0.33}D_{2.0}$ and $Al_{0.10}Ti_{0.30}V_{0.30}Nb_{0.30}D_{1.6}$ at room temperature are plotted in Figure 5 together with the related Rietveld refinements. Both deuterides crystallize in a *fcc* lattice (Fm-3m) as the dihydride phases, with the parameter a_{fcc} = 4.432(1) Å and a_{fcc} = 4.358(1) Å for $Ti_{0.33}V_{0.33}Nb_{0.33}D_{2.0}$ and $Al_{0.10}Ti_{0.30}V_{0.30}Nb_{0.30}D_{1.6}$, respectively (Table 1). Moreover, a full occupation of deuterium atoms in the tetrahedral sites of the *fcc* lattice is verified for both compositions, which is in good agreement with previous results [26,28].

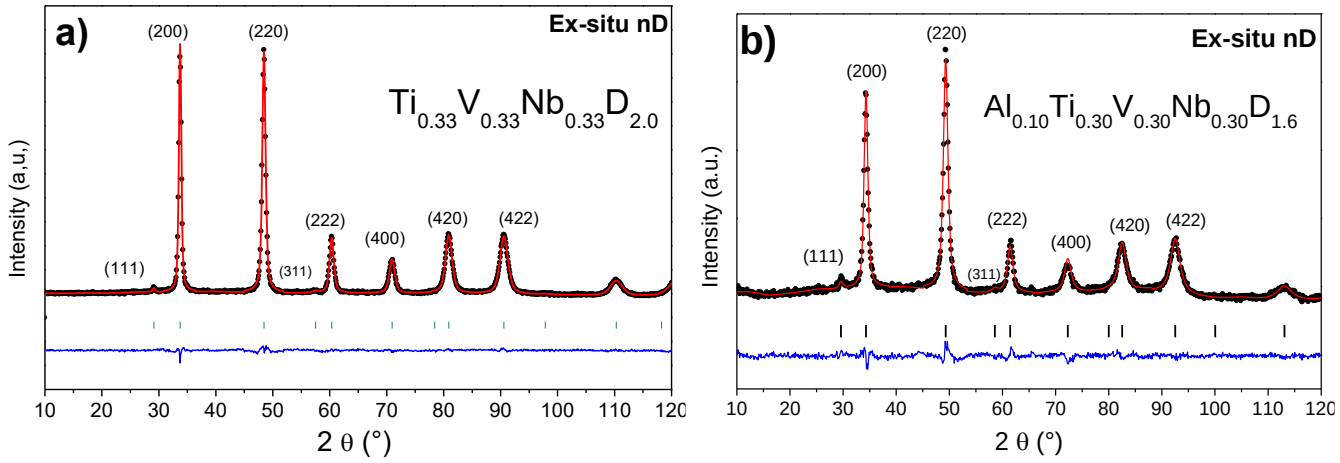

Figure 5. *Ex-situ neutron diffraction patterns (λ=1.28 Å) of the fully deuterated samples, a) $Ti_{0.33}V_{0.33}Nb_{0.33}D_{2.0}$ and b) $Al_{0.10}Ti_{0.30}V_{0.30}Nb_{0.30}D_{1.6}$.*

The desorption properties of the hydrides/deuterides have been determined by thermo-desorption spectroscopy (TDS with a heating rate of 5°C/min) and by *in-situ* neutron diffraction (nD with a heating rate of 1°C/min) under dynamic secondary vacuum conditions. The TDS profile of $Ti_{0.33}V_{0.33}Nb_{0.33}H_{2.0}$ (Figure 6.a) shows a sharp main event at 236 °C with the onset temperature of desorption around 215 °C. This main desorption peak is followed by a large desorption peak at higher temperature ending around 400 °C. The same desorption profile was reported previously for the equimolar TiVNb alloy with the onset temperature at 280 °C and the maximum temperature of the main desorption peak at around 290 °C [21]. According to Nygård *et al*. the first desorption peak is attributed to the transition from the *fcc* dihydride to the *bcc* monohydride and the second large peak to the final transformation of the *bcc* monohydride into the desorbed *bcc* alloy [21].

The $Al_{0.10}Ti_{0.30}V_{0.30}Nb_{0.30}H_{1.6}$ shows two main TDS events at lower temperature than the ternary composition: the first desorption is a flat-like broad event with the onset temperature at 77 °C followed by a second sharp peak with maximum at 210 °C which ends at around 300 °C (Figure 6.b). Clearly the presence of Al drastically reduces the temperature of desorption, in line with our earlier results on the comparison between Ti-V-Zr-Nb and Al-containing counterpart [17].

The desorbed materials crystallize in a *bcc* phase with the lattice parameters (calculated with CELREF software) very similar to the ones of the as-cast alloys (Table 1), as proven by XRD. This confirms that the hydrogen absorption and desorption are fully reversible for both compositions. *In-situ* neutron thermo-diffractogram of $Ti_{0.33}V_{0.33}Nb_{0.33}D_{2.0}$ and $Al_{0.10}Ti_{0.30}V_{0.30}Nb_{0.30}D_{1.6}$ during deuterium desorption along with the vacuum pressure readings are shown in Figure 6.c and 6.d, respectively. The initial *fcc* structure (marked with #) of the $Ti_{0.33}V_{0.33}Nb_{0.33}D_{2.0}$ shows good thermal stability up to around 220°C (Figure 6.c). Above this temperature, the intensity of the *fcc* peaks gradually decreases and completely disappears at around 260 °C while the desorption profile shows a

main peak with a maximum at 241 °C. The material undergoes a sharp transition during desorption of deuterium at around 220 °C and a new *bcc* phase with weak diffraction peaks (marked with *) is formed above 240 °C. Moreover, the *bcc* peaks shift to higher 2θ with the temperature increase, which implies a shrinking of the lattice parameters with heating *i.e.*, the sample continues to desorb deuterium from the *bcc* phase above 240 °C.

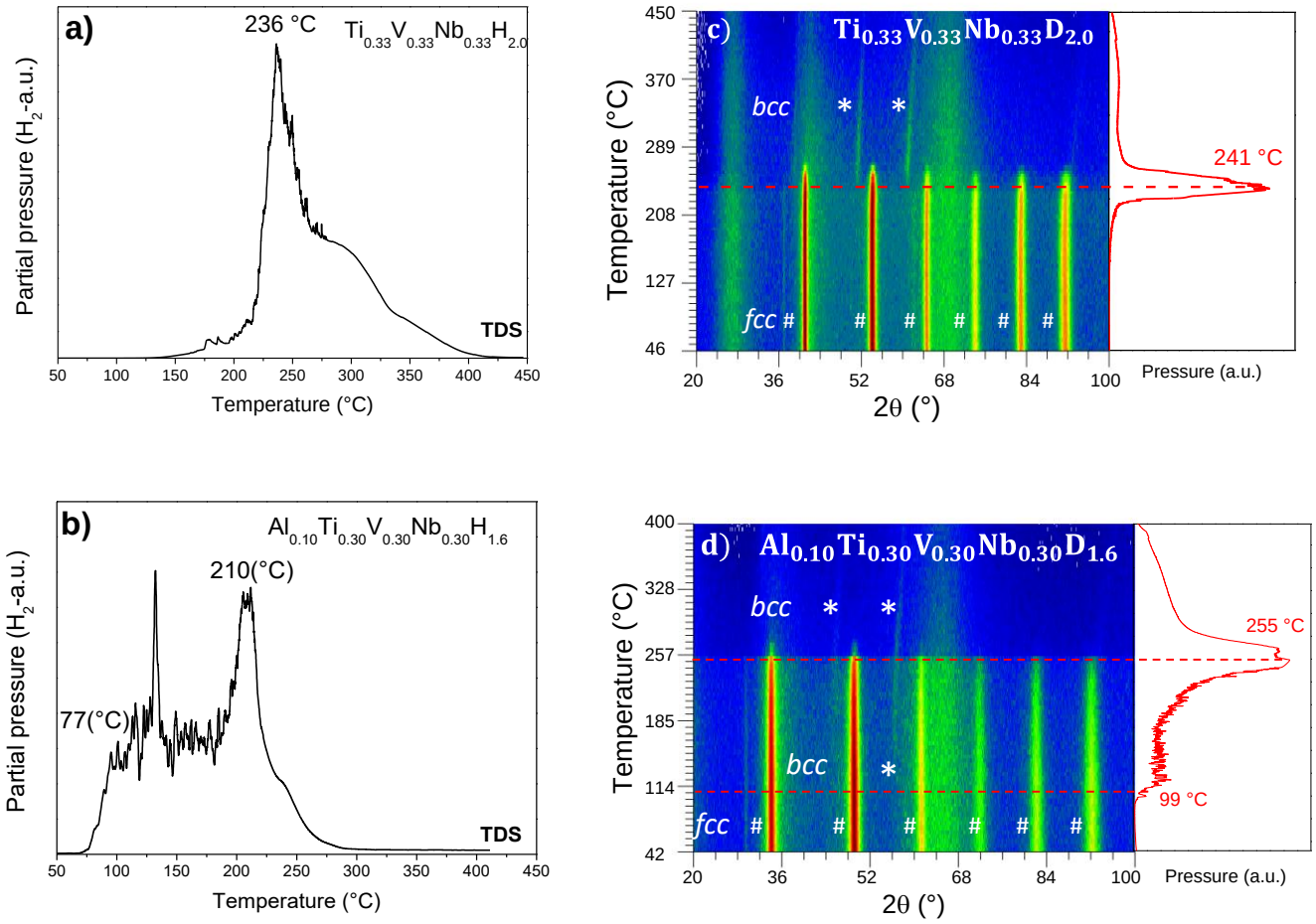

Figure 6. *Thermo-desorption spectroscopy (TDS) spectra of a) $Ti_{0.33}V_{0.33}Nb_{0.33}H_{2.0}$ and b) $Al_{0.10}Ti_{0.30}V_{0.30}Nb_{0.30}H_{1.6}$ (heating ramp of 5°C/min). In-situ neutron diffraction (nD) on the left and the corresponding desorption profile on the right of c) $Ti_{0.33}V_{0.33}Nb_{0.33}D_{2.0}$ and d) $Al_{0.10}Ti_{0.30}V_{0.30}Nb_{0.30}D_{1.6}$ (heating ramp of 1°C /min).*

The *in-situ* neutron thermo-diffractogram of $Al_{0.10}Ti_{0.30}V_{0.30}Nb_{0.30}D_{1.6}$ proves that the initial *fcc* deuteride (marked with #) is stable up to around 100°C (Figure 6.d). Above this temperature, a desorption event occurs with the formation of a *bcc* phase with very weak intensity (marked with *).

Both *fcc* and *bcc* phases coexist up to around 255 °C where a main desorption event occurs, noticed as a sharp peak in the desorption profile, accompanied by the complete fading of the *fcc* hydride. Above 255 °C only the two main peaks of the *bcc* phase are observed with lesser intensity. The weak intensities of the diffraction peaks of the *bcc* phases obtained after desorption from both $Ti_{0.33}V_{0.33}Nb_{0.33}D_{2.0}$ and $Al_{0.10}Ti_{0.30}V_{0.30}Nb_{0.30}D_{1.6}$ compositions are due to the low neutron cross-section of the desorbed material (the alloys without deuterium). Previously, it has been reported that refractory high entropy alloys are highly transparent to thermal neutron beams [4] and thus are interesting candidates as cladding materials for nuclear reactors [29]. Overall, the *in-situ* nD results are in good agreement with the laboratory TDS analysis for both compositions, despite some discrepancies in the recorded temperatures of the desorption events, which can be related to the different heating rates and sample environments.

It is clear from these experiments that the addition of 10 at.% Al into $Ti_{0.33}V_{0.33}Nb_{0.33}$ drastically reduces the onset desorption temperature (from 215 to 77 °C), and consequently the formation of the desorbed *bcc* phase starts progressively at low temperature and the desorption process is less abrupt compared to the ternary composition. This remarkable decrease of the desorption temperature was also observed earlier for the 10 at.% Al addition in the the quaternary alloy $Ti_{0.325}V_{0.275}Zr_{0.125}Nb_{0.275}$ [17].

Lastly, both alloys were submitted to around 10-11 hydrogen absorption/desorption cycles to evaluate their reversible storage capacity. The cycling assessment consisted of measuring the hydrogen absorption kinetics at 25°C under 60 bar H_2 followed by complete hydrogen desorption by heating at 400 °C while evacuating under secondary vacuum for 12 hours. The kinetic results and the capacity variation over cycling are presented in Figure 7 for both compositions. It can be observed that in the first cycle full capacity is reached in less than 10 and 30 minutes for $Ti_{0.33}V_{0.33}Nb_{0.33}$ and $Al_{0.10}Ti_{0.30}V_{0.30}Nb_{0.30}$, respectively. For subsequent cycles the absorption kinetics improves reaching maximum capacity in less than 1 minute, irrespective of composition. However, it is important to notice

that in the ternary alloy, the capacity decreases by around 12 % after the first cycle (2.0 H/M) and stabilizes to around 1.75 H/M for further cycles.

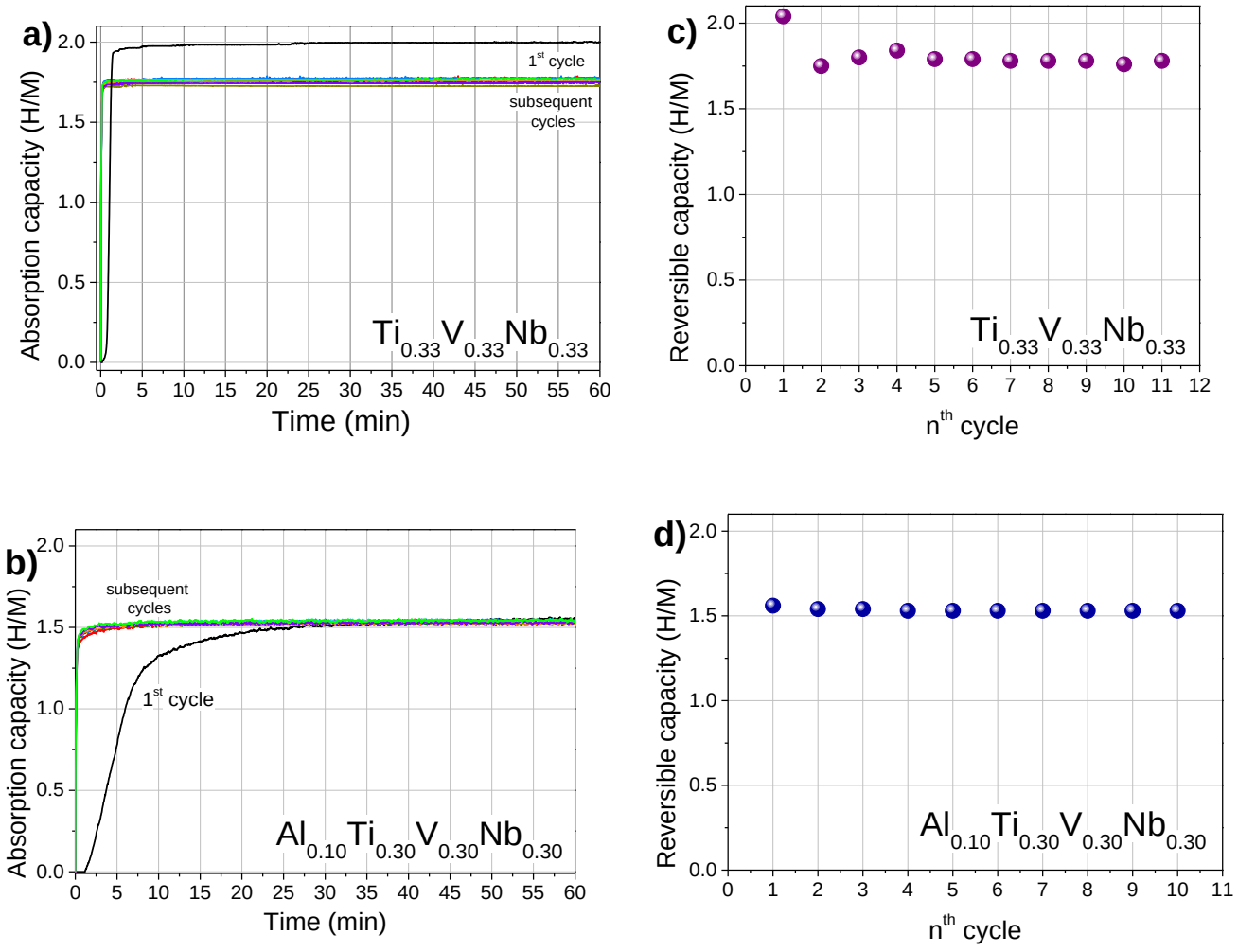

Figure 7. *Kinetics of absorption over 10-11 cycles at 25°C of a) $Ti_{0.33}V_{0.33}Nb_{0.33}$ and b) $Al_{0.10}Ti_{0.30}V_{0.30}Nb_{0.30}$. The variation of the absorption capacity at 25°C and desorption at 400°C of c) $Ti_{0.33}V_{0.33}Nb_{0.33}$ and d) $Al_{0.10}Ti_{0.30}V_{0.30}Nb_{0.30}$.*

On the contrary, the capacity over cycling in the quaternary composition is stable and shows only a minor reduction in the first cycle from approximately 1.56 H/M to around 1.53 H/M. Similar effects due to Al addition on the cycling properties were also noticed in $Ti_{0.325}V_{0.275}Zr_{0.125}Nb_{0.275}$ [17]. Both materials form a stable single-phase *fcc* dihydride after 10 cycles with similar lattice parameter (calculated with CELREF software) as the initial alloys (Table 1). Moreover, the chemical mapping by EDX-SEM after cycling of $Ti_{0.33}V_{0.33}Nb_{0.33}H_{1.8}$ (Figure SI1) and $Al_{0.10}Ti_{0.30}V_{0.30}Nb_{0.30}H_{1.53}$ (Figure SI2)

shows the same microstructure without phase segregation that might be induced by progressive cycling. The overall chemical composition is unchanged after cycling (Tables 3 and 4) demonstrating a good chemical stability for both alloys. Overall, these results agree very well the behaviour observed in Ti-V-Zr-Nb with the addition of a light metal such as Al [17] and Mg [5], as reported previously.

CONCLUSIONS

The modifications of hydrogen storage properties *via* 10 at.% Al addition in the equimolar TiVNb have been thoroughly elucidated, including several that are favourable for practical storage applications. The as-prepared $Ti_{0.33}V_{0.33}Nb_{0.33}$ and $Al_{0.10}Ti_{0.30}V_{0.30}Nb_{0.30}$ are single-phased *bcc* alloys which behave similarly toward hydrogen. The maximum capacity reduces with Al addition from 2.0 to 1.6 H/M in the ternary and quaternary alloys, respectively. Both alloys show a two-step reaction during hydrogen absorption from *bcc* solid solution → *bcc* monohydride → *fcc* dihydride. Moreover, the first plateau in the PCI curves occurs at very low pressure, whereas the second is at high pressure. The thermodynamic properties for the second transition (*bcc* monohydride → *fcc* dihydride) have been experimentally determined and compared to ML predictions. Both approaches reveal a destabilization of the hydride. Importantly, this reinforces the utility of the ML model to identify destabilized MPEA hydrides for experimental realization in future materials discovery exercises. Furthermore, a flattening of the PCI plateaus by Al addition in the equimolar TiVNb was observed. Neutron diffraction experiments have clarified the occupancy of the deuterium atoms in the tetrahedral sites of the *fcc* dihydride lattice, irrespective of the composition. Moreover, the Al addition in TiVNb drastically influences the hydrogen desorption properties: the desorption events shift to lower temperature with an onset temperature of desorption below 100 °C, as proven by two distinct experimental techniques, thermo-desorption-spectroscopy and *in situ* neutron diffraction. The absorption/desorption cycling properties are improved by Al addition to the equimolar TiVNb. The quaternary alloy shows an excellent stability and reversibility during cycling. Furthermore, no phase segregation or any chemical

inhomogeneities could be noticed after 10 cycles. Based on the present results, Al addition in refractory MPEAs seems to be a good comprise to improve the design novel alloys with tuneable properties for specific applications.

SUPPLEMENTARY MATERIALS: The following supporting is available: Figure SI1. Chemical mapping analysis by EDX-SEM of the hydride $Ti_{0.33}V_{0.33}Nb_{0.33}H_{1.8}$ after 11 absorption/desorption cycles; Figure SI2. Chemical mapping analysis by EDX-SEM of the hydride $Al_{0.10}Ti_{0.30}V_{0.30}Nb_{0.30}H_{1.5}$ after 10 cycles; Figure SI3. Machine learning model predictions of both desorption enthalpy, ΔH, and maximum H/M capacity, as a function of Al at. % in the AlxTizVzNbz [z=(100-x)/3]. Figure SI4. Rietveld refinement analysis of the X-Ray diffraction (XRD) patterns (λ = 1.5406Å) for the (a) *fcc* $Ti_{0.33}V_{0.33}Nb_{0.33}H_{2.0}$ dihydride and (b) *fcc* $Al_{0.10}Ti_{0.30}V_{0.30}Nb_{0.30}H_{1.6}$ dihydride.

AUTHOR CONTRIBUTIONS

Conceptualization: C.Z.; Formal analysis: N.P.R., M.W. and C.Z.; Investigation, Methodology: N.P.R. and C.Z.; Supervision, Validation: C.Z.; Writing original draft: N.P.R. and C.Z.; Writing - review & editing, N.P.R., C.Z., M.W., V.S.

FUNDING

This research was funded by ANR MASSHY project ANR-19-CE05-0029-01.

ACKNOWLEDGMENTS

We acknowledge ILL for beamtime allocation on the CRG-D1B beamline. CZ acknowledge Laetitia Laversenne, Vivian Nassif from Institute Néel as well as Anis Bouzidi and Fabrice Couturas from ICMPE for help during neutron diffraction at ILL. CZ and NPR thank Loïc Perrière for help with arc melting. The French National Research Agency (ANR) is acknowledged for the financial support in the frame of the MASSHY project (ANR-19-CE05-0029-01). MW and VS gratefully acknowledge research support

from the U.S. Department of Energy, Office of Energy Efficiency and Renewable Energy, Fuel Cell Technologies Office through the Hydrogen Storage Materials Advanced Research Consortium (HyMARC). This work was also supported by the Laboratory Directed Research and Development program at Sandia National Laboratories. Sandia National Laboratories is a multimission laboratory managed and operated by National Technology & Engineering Solutions of Sandia, LLC, a wholly owned subsidiary of Honeywell International Inc., for the U.S. Department of Energy's National Nuclear Security Administration under contract DE-NA0003525. This paper describes objective technical results and analysis. Any subjective views or opinions that might be expressed in the paper do not necessarily represent the views of the U.S. Department of Energy or the United States Government.

REFERENCES

[1] M. Hirscher, V.A. Yartys, M. Baricco, J. Bellosta von Colbe, D. Blanchard, R.C. Bowman, D.P. Broom, C.E. Buckley, F. Chang, P. Chen, Y.W. Cho, J.-C. Crivello, F. Cuevas, W.I.F. David, P.E. de Jongh, R.V. Denys, M. Dornheim, M. Felderhoff, Y. Filinchuk, G.E. Froudakis, D.M. Grant, E.MacA. Gray, B.C. Hauback, T. He, T.D. Humphries, T.R. Jensen, S. Kim, Y. Kojima, M. Latroche, H.-W. Li, M.V. Lototskyy, J.W. Makepeace, K.T. Møller, L. Naheed, P. Ngene, D. Noréus, M.M. Nygård, S. Orimo, M. Paskevicius, L. Pasquini, D.B. Ravnsbæk, M. Veronica Sofianos, T.J. Udovic, T. Vegge, G.S. Walker, C.J. Webb, C. Weidenthaler, C. Zlotea, Materials for hydrogen-based energy storage – past, recent progress and future outlook, J. Alloys Compd. 827 (2020) 153548. https://doi.org/10.1016/j.jallcom.2019.153548.

[2] L.J. Bannenberg, M. Heere, H. Benzidi, J. Montero, E.M. Dematteis, S. Suwarno, T. Jaroń, M. Winny, P.A. Orłowski, W. Wegner, A. Starobrat, K.J. Fijałkowski, W. Grochala, Z. Qian, J.-P. Bonnet, I. Nuta, W. Lohstroh, C. Zlotea, O. Mounkachi, F. Cuevas, C. Chatillon, M. Latroche, M. Fichtner, M. Baricco, B.C. Hauback, A. El Kharbachi, Metal (boro-) hydrides for high energy density storage and relevant emerging technologies, Int. J. Hydrog. Energy. 45 (2020) 33687–33730. https://doi.org/10.1016/j.ijhydene.2020.08.119.

[3] F. Marques, M. Balcerzak, F. Winkelmann, G. Zepon, M. Felderhoff, Review and outlook on high-entropy alloys for hydrogen storage, Energy Environ. Sci. 14 (2021) 5191-5227. https://doi.org/10.1039/D1EE01543E.

[4] M. Sahlberg, D. Karlsson, C. Zlotea, U. Jansson, Superior hydrogen storage in high entropy alloys, Sci. Rep. 6 (2016) 36770. https://doi.org/10.1038/srep36770.

[5] J. Montero, G. Ek, M. Sahlberg, C. Zlotea, Improving the hydrogen cycling properties by Mg addition in Ti-V-Zr-Nb refractory high entropy alloy, Scr. Mater. 194 (2021) 113699. https://doi.org/10.1016/j.scriptamat.2020.113699.

[6] J. Montero, G. Ek, L. Laversenne, V. Nassif, G. Zepon, M. Sahlberg, C. Zlotea, Hydrogen storage properties of the refractory Ti–V–Zr–Nb–Ta multi-principal element alloy, J. Alloys Compd. 835 (2020) 155376. https://doi.org/10.1016/j.jallcom.2020.155376.

[7] J. Montero, C. Zlotea, G. Ek, J.-C. Crivello, L. Laversenne, M. Sahlberg, TiVZrNb Multi-Principal-Element Alloy: Synthesis Optimization, Structural, and Hydrogen Sorption Properties, Molecules. 24 (2019) 2799. https://doi.org/10.3390/molecules24152799.
[8] C. Zlotea, M.A. Sow, G. Ek, J.-P. Couzinié, L. Perrière, I. Guillot, J. Bourgon, K.T. Møller, T.R. Jensen, E. Akiba, M. Sahlberg, Hydrogen sorption in TiZrNbHfTa high entropy alloy, J. Alloys Compd. 775 (2019) 667–674. https://doi.org/10.1016/j.jallcom.2018.10.108.
[9] F. Schüth, M. Felderhoff, U. Eberle, Chemical and Physical Solutions for Hydrogen Storage, Angew. Chem. 48 (2009) 6608–6630. https://doi.org/10.1002/anie.200806293.
[10] R.B. Strozi, D.R. Leiva, J. Huot, W.J. Botta, G. Zepon, Synthesis and hydrogen storage behavior of Mg–V–Al–Cr–Ni high entropy alloys, Int. J. Hydrog. Energy. 46 (2021) 2351–2361. https://doi.org/10.1016/j.ijhydene.2020.10.106.
[11] G. Zepon, D.R. Leiva, R.B. Strozi, A. Bedoch, S.J.A. Figueroa, T.T. Ishikawa, W.J. Botta, Hydrogen-induced phase transition of MgZrTiFe0.5Co0.5Ni0.5 high entropy alloy, Int. J. Hydrog. Energy. 43 (2018) 1702–1708. https://doi.org/10.1016/j.ijhydene.2017.11.106.
[12] F. Marques, H.C. Pinto, S.J.A. Figueroa, F. Winkelmann, M. Felderhoff, W.J. Botta, G. Zepon, Mg-containing multi-principal element alloys for hydrogen storage: A study of the MgTiNbCr0.5Mn0.5Ni0.5 and Mg0.68TiNbNi0.55 compositions, Int. J. Hydrog. Energy. 45 (2020) 19539–19552. https://doi.org/10.1016/j.ijhydene.2020.05.069.
[13] J. Graetz, J.J. Reilly, V.A. Yartys, J.P. Maehlen, B.M. Bulychev, V.E. Antonov, B.P. Tarasov, I.E. Gabis, Aluminum hydride as a hydrogen and energy storage material: Past, present and future, J. Alloys Compd. 509 (2011) S517–S528. https://doi.org/10.1016/j.jallcom.2010.11.115.
[14] N.D. Stepanov, D.G. Shaysultanov, G.A. Salishchev, M.A. Tikhonovsky, Structure and mechanical properties of a light-weight AlNbTiV high entropy alloy, Mater. Lett. 142 (2015) 153–155. https://doi.org/10.1016/j.matlet.2014.11.162.
[15] S.Y. Chen, X. Yang, K.A. Dahmen, P.K. Liaw, Y. Zhang, Microstructures and Crackling Noise of AlxNbTiMoV High Entropy Alloys, Entropy. 16 (2014) 870–884. https://doi.org/10.3390/e16020870.
[16] O.N. Senkov, S.V. Senkova, C. Woodward, Effect of aluminum on the microstructure and properties of two refractory high-entropy alloys, Acta Mater. 68 (2014) 214–228. https://doi.org/10.1016/j.actamat.2014.01.029.
[17] J. Montero, G. Ek, L. Laversenne, V. Nassif, M. Sahlberg, C. Zlotea, How 10 at% Al Addition in the Ti-V-Zr-Nb High-Entropy Alloy Changes Hydrogen Sorption Properties, Molecules. 26 (2021) 2470. https://doi.org/10.3390/molecules26092470.
[18] M. Witman, G. Ek, S. Ling, J. Chames, S. Agarwal, J. Wong, M.D. Allendorf, M. Sahlberg, V. Stavila, Data-Driven Discovery and Synthesis of High Entropy Alloy Hydrides with Targeted Thermodynamic Stability, Chem. Mater. 33 (2021) 4067–4076. https://doi.org/10.1021/acs.chemmater.1c00647.
[19] M. Witman, S. Ling, D.M. Grant, G.S. Walker, S. Agarwal, V. Stavila, M.D. Allendorf, Extracting an Empirical Intermetallic Hydride Design Principle from Limited Data via Interpretable Machine Learning, J. Phys. Chem. Lett. 11 (2020) 40–47. https://doi.org/10.1021/acs.jpclett.9b02971.
[20] C. Zlotea, Y. Oumellal, M. Msakni, J. Bourgon, S. Bastide, C. Cachet-Vivier, M. Latroche, First Evidence of Rh Nano-Hydride Formation at Low Pressure, Nano Lett. 15 (2015) 4752–4757. https://doi.org/10.1021/acs.nanolett.5b01766.
[21] M.M. Nygård, G. Ek, D. Karlsson, M.H. Sørby, M. Sahlberg, B.C. Hauback, Counting electrons - A new approach to tailor the hydrogen sorption properties of high-entropy alloys, Acta Mater. 175 (2019) 121–129. https://doi.org/10.1016/j.actamat.2019.06.002.
[22] D.B. Miracle, O.N. Senkov, A critical review of high entropy alloys and related concepts, Acta Mater. 122 (2017) 448–511. https://doi.org/10.1016/j.actamat.2016.08.081.
[23] X. Yang, Y. Zhang, Prediction of high-entropy stabilized solid-solution in multi-component alloys, Mater. Chem. Phys. 132 (2012) 233–238. https://doi.org/10.1016/j.matchemphys.2011.11.021.

[24] S. Yang, J. Lu, F. Xing, L. Zhang, Y. Zhong, Revisit the VEC rule in high entropy alloys (HEAs) with high-throughput CALPHAD approach and its applications for material design-A case study with Al–Co–Cr–Fe–Ni system, Acta Mater. 192 (2020) 11–19. https://doi.org/10.1016/j.actamat.2020.03.039.
[25] B.H. Silva, C. Zlotea, Y. Champion, W.J. Botta, G. Zepon, Design of TiVNb-(Cr, Ni or Co) multicomponent alloys with the same valence electron concentration for hydrogen storage, J. Alloys Compd. 865 (2021) 158767. https://doi.org/10.1016/j.jallcom.2021.158767.
[26] G. Ek, M.M. Nygård, A.F. Pavan, J. Montero, P.F. Henry, M.H. Sørby, M. Witman, V. Stavila, C. Zlotea, B.C. Hauback, M. Sahlberg, Elucidating the Effects of the Composition on Hydrogen Sorption in TiVZrNbHf-Based High-Entropy Alloys, Inorg. Chem. 60 (2021) 1124–1132. https://doi.org/10.1021/acs.inorgchem.0c03270.
[27] M.M. Nygård, Ø.S. Fjellvåg, M.H. Sørby, K. Sakaki, K. Ikeda, J. Armstrong, P. Vajeeston, W.A. Sławiński, H. Kim, A. Machida, Y. Nakamura, B.C. Hauback, The average and local structure of TiVCrNbDx (x=0,2.2,8) from total scattering and neutron spectroscopy, Acta Mater. 205 (2021) 116496. https://doi.org/10.1016/j.actamat.2020.116496.
[28] M.M. Nygård, W.A. Sławiński, G. Ek, M.H. Sørby, M. Sahlberg, D.A. Keen, B.C. Hauback, Local order in high-entropy alloys and associated deuterides – a total scattering and Reverse Monte Carlo study, Acta Mater. 199 (2020) 504–513. https://doi.org/10.1016/j.actamat.2020.08.045.
~~[29] M. Sahlberg, D. Karlsson, C. Zlotea, U. Jansson, Superior hydrogen storage in high entropy alloys, Sci. Rep. 6 (2016) 36770.~~
[29] D.J.M. King, S.T.Y. Cheung, S.A. Humphry-Baker, C. Parkin, A. Couet, M.B. Cortie, G.R. Lumpkin, S.C. Middleburgh, A.J. Knowles, High temperature, low neutron cross-section high-entropy alloys in the Nb-Ti-V-Zr system, Acta Mater. 166 (2019) 435–446. https://doi.org/10.1016/j.actamat.2019.01.006.